Key Engineering Materials
ISSN: 1662-9795, Vol. 1047, pp 21-29

Submitted: 2025-12-04
Accepted: 2026-02-11
Online: 2026-04-13

A Comparative Analysis of LPBF Process Maps for S2 and S6 Grades Tool Steel

Segatto Alessandra[1,a], Saggionetto Enrico[1,b], Dedry Olivier[1,c], Tchuindjang Jérôme Tchoufang[1,d] and Mertens Anne[1,e*]

[1]Metallic Materials for Additive Manufacturing (MMS), Aerospace and Mechanical Engineering Dpt., University of Liège – Quartier POLYTECH1, Allée de la Découverte 9 – 4000 Liège (Belgium)

[a]alessandra.segatto@uliege.be, [b]enrico.saggionetto@liege.be, [c]olivier.dedry@uliege.be, [d]j.tchuindjang@uliege.be, [e*]anne.mertens@uliege.be

[*]corresponding author: anne.mertens@uliege.be

Keywords: LPBF, tool steel, processing map.

Abstract. Laser Powder Bed Fusion (LPBF) represents a significant advancement in metal additive manufacturing, facilitating the near-net-shape fabrication of intricate, high-performance tool-steel components. This process is accomplished through a layer-by-layer selective melting technique and extremely rapid solidification (ranging from 10^3 to 10^6 K/s). The establishment of process maps-both empirical and predictive frameworks that correlate variables such as laser power, scan speed, and defect thresholds - is crucial for defining processing windows and optimising parameter selection. In tool steels, the influence of alloying elements is significant as they affect solidification behaviour, phase stability, and susceptibility to cracking. Carbide-forming additions can constrict the defect-free range, while stabilising elements can enhance toughness and dimensional accuracy. This study aims to develop a process map for S6 tool steel by varying laser scan speed and laser power. Small cubes are printed using various combinations of these parameters, followed by microstructural characterisation of the as-built material. This characterisation will include optical microscopy (OM) and porosity assessment. After establishing the process map for S6, the resulting microstructures are compared with those previously characterised for LPBF-processed S2 tool steel. This comparison provides valuable insight into the differences in the as-built microstructures of LPBF S2 and LPBF S6, particularly in relation to how the presence and relative amounts of alloying elements influence processability and microstructural development.

Introduction

Laser Powder Bed Fusion (LPBF) is a prevalent additive manufacturing (AM) technique known for its capability to produce high-performance metallic components characterised by complex geometries and near-net-shape accuracy. The layer-by-layer fabrication inherent to LPBF facilitates exceptional design freedom and efficient material utilisation, making it particularly advantageous for tool steels and high-strength alloys [1, 2]. Nevertheless, the intrinsic characteristics associated with LPBF - such as localised melting, rapid solidification, and the development of thermal gradients - present notable challenges in processing systems, particularly in relation to susceptibility to cracking and segregation [3]. Tool steels, in particular, are recognised as some of the most challenging materials to process successfully due to their high hardenability, substantial carbon content, and broad solidification temperature range [4].

Previous research has established that parameters including laser power, scanning speed, hatch spacing, and layer thickness are critical in determining melt pool stability, porosity, and microstructural outcomes [5, 6]. Despite the advancements in understanding these parameters, certain grades of shock-resisting steels, such as S2 and S6, have received relatively limited attention compared to other tool steel variants [7].

From a metallurgical standpoint, S2 and S6 tool steels are classified as shock-resisting steels, engineered to achieve a balance between moderate hardness and high toughness when subjected to dynamic loads. S2 features elevated carbon and silicon contents that contribute to a fine martensitic

matrix and enhanced compressive strength; however, these same qualities may lead to an increased vulnerability to cracking due to diminished thermal conductivity. Conversely, S6 incorporates higher levels of manganese and chromium, enhancing toughness and mitigating quench sensitivity (Table 1). It is crucial to comprehend these distinctions to establish process windows that promote consistent densification and microstructural homogeneity across both grades.

Recent advancements have seen the emergence of process maps (Figure 4) as an effective means to describe and visualise the processability of alloys in LPBF [8, 9]. These maps correlate critical process parameters with performance outcomes, such as relative density, surface roughness, and microstructural stability, facilitating the identification of stable processing windows. Initial works have suggested the development of process maps for various materials, including stainless steels and nickel-based superalloys, often supported by empirical optimisation and melt pool modelling [10, 11]. However, there remains a notable gap in the literature regarding process maps for tool steels, particularly for S6.

The integration of parameters for process mapping presents a dual benefit: it enables the identification of stable regions for achieving fully dense and defect-free consolidations while providing a physical explanation for divergences observed among alloys [11]. This approach is especially pertinent for tool steels, where processing windows are frequently narrow and sensitive to both thermal and metallurgical variables [12].

This study seeks to address the existing gap by undertaking a comparative investigation of the LPBF process maps for S2 and S6 tool steels. A systematic parameter study will be conducted to construct process maps that correlate laser power and scanning speed with relative density. The resulting samples will be examined using optical microscopy (OM), scanning electron microscopy (SEM), and surface profilometry to assess mechanisms of densification, defect formation, and melt track morphology. This research aims to establish a direct comparison between the LPBF processability of S2 and S6 tool steels, linking elemental differences to resultant microstructural and surface characteristics. The findings aspire to enhance the understanding of process-structure relationships in shock-resisting tool steels and serve as a foundation for optimising processing parameters across various alloy grades. Furthermore, the methodology proposed—integrating process mapping with microstructural evaluation—presents a transferable framework for evaluating similarly challenging alloys in the additive manufacturing landscape.

Materials and Methods

Process map of S2 tool steel was previously studied [13]. Commercial powder of S6 tool steel were supplied by Sandvik Osprey LTD. The nominal composition of both steels is given in Table 1.

Table 1. Nominal composition of S6 and S2 tool steel powders.

%wt	C	Si	Mn	Cr	Mo	V	Fe
S6	0.31	2.1	1.1	1.7	0.4	0.37	Bal.
S2	0.49	1.2	0.60	-	0.60	-	Bal.

A total of 20 cubes, of 10x10x10 mm³ sizes, were produced using an Aconity MINI LPBF printer under Argon atmosphere. In comparison to the printer used in the study on S2 grade [13], this LPBF printer utilizes a reduced set of printing parameters. Table 2 shows the different values of laser powers (P) and scan velocities (Vs) used. Those parameters were selected based on the S2 samples results [13]. A laser spot of 80 µm with a gaussian distribution, a layer thickness (t) of 30 µm and a hatch spacing (h) of 80 µm were used for all samples. The scanning strategy was set as a 90° rotation for each layer, without contouring. The volumetric energy density (Ed) was calculated based on the processing parameters (Eq. 1).

$$Ed = \frac{P}{t*h*vs} \quad (1)$$

The surface of the as-built samples was checked using an Alicona Infinite Focus G5 optical profilometer for roughness analysis. All the as-built samples were cut by Electro Discharge

Machining perpendicularly to the laser scan direction of the last layer, to obtain the vertical cross section. After cutting, samples were hot mounted with an electrically conductive resin, then ground and polished down to 1 μm. Samples were etched with 3% Nital to reveal specific microstructural features. Defects and porosity within the cross sections were examined using an optical microscope (OM - Olympus BX60). The porosity assessment through the optical microscope analysed the selected cross section and provided a percentage measurement of porosity.

Table 2. Parameters of printing S6 tool steel.

Sample	P [w]	Vs [mm/s]	Ed [J/mm^3]	Print completed
1	125	200	260	Yes
2	125	400	130	Yes
3	125	600	87	Yes
4	125	800	65	Yes
5	150	400	156	No
6	150	600	104	Yes
7	150	800	78	Yes
8	150	1000	63	Yes
9	175	400	182	No
10	175	600	122	No
11	175	800	91	Yes
12	175	1000	73	Yes
13	175	1500	49	Yes
14	200	400	208	No
15	200	600	139	No
16	200	800	104	No
17	200	1000	83	Yes
18	200	1200	69	Yes
19	200	1500	56	Yes
20	200	2000	42	yes

Results and Discussion

Profilometer analyses

The printing was not completed for samples 5, 9, 10, 14, 15, and 16 due to excessive spatters and defects detected during printing (Table 2). Figure 1 presents an example of profilometer measurements (from sample 2). Figure 2 shows the results for the surface roughness (Sa); additionally, the largest difference between maximum peak height and maximum valley depth was recorded for sample 3 (-181.07 μm). No relation between Sa and Ed was detected. After cutting, the samples were analysed with an optical microscope. Porosity measurements through OM are reported in Table 3. The best results of Sa are related to the best in terms of porosity, while the worst samples for Sa (i.e. samples 2, 3, 6) are related to the worst in terms of porosity.

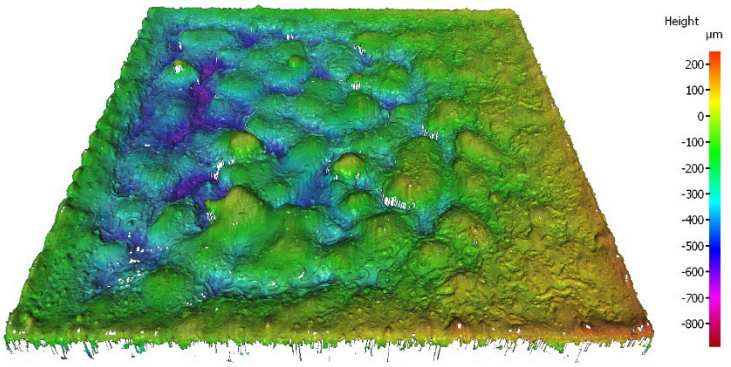

Fig. 1. Typical surface topography as obtained from profilometer measurement for sample 2.

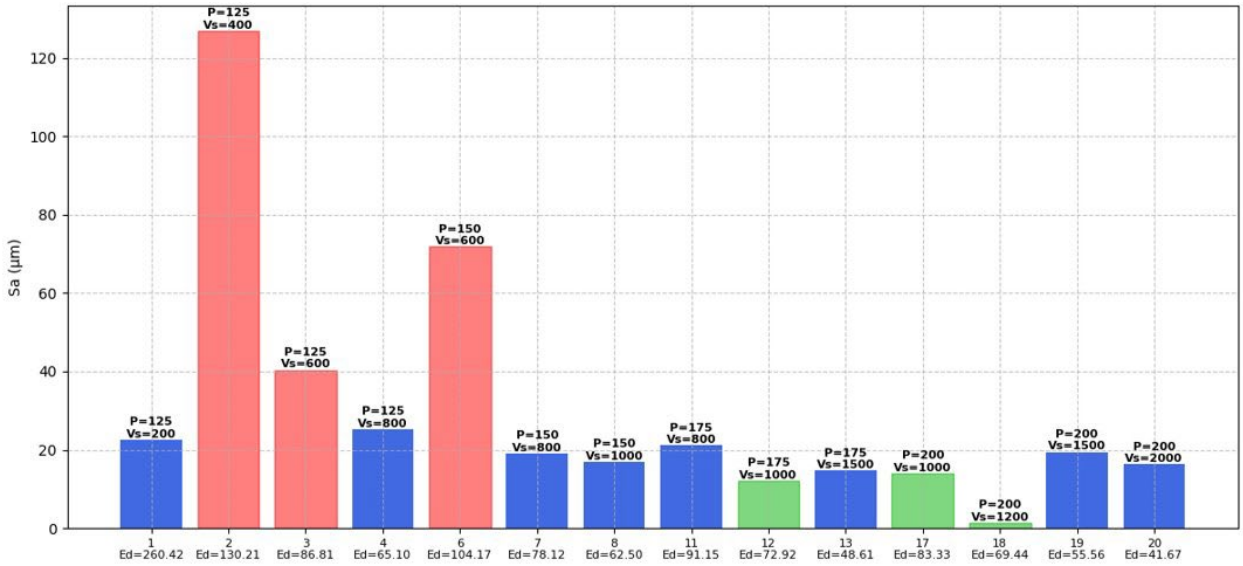

Fig. 2. Surface roughness (Sa) results. In red, the three worst results; in green, the three best results.

Printing defects

The porosity measurements and images are reported in Table 3, using the same red and green contours as in Figure 2.
The type of defects identified through porosity assessments and analysed in optical micrographs, as detailed in Table 4, are summarised in Table 3.

Table 3. Types of defects confronted and the specific samples in which they are present.

Type of defects	Sample present
Keyhole porosity	1, 11, 12, 13
Cold cracks	1, 7, 8
Lack of fusion	2, 3, 4, 6, 7, 8, 19, 20

The defects outlined in Table 3 represent common issues observed in LPBF printed samples. Keyhole porosity has been previously documented [10, 14], while cold cracks have been described [15, 16]. Cold cracks result from high internal stresses and sharp thermal gradients that develop during the cooling and solidification processes. In contrast, keyhole porosities are associated with excessive energy input: when the laser power is excessively high or the scan speed is too low, intense metal evaporation can create a deep vapour cavity. If this keyhole becomes unstable, it may oscillate and collapse, trapping gas within the solidifying melt pool, leading to the formation of spherical or near-spherical pores. The evaporation of volatile alloying elements like manganese, silicon, or chromium in tool steels can further aggravate plume formation, thereby increasing keyhole instability.
Another persistent defect is a lack of fusion, which has already been analysed by [17]. This defect occurs when the laser energy is insufficient to fully melt both the powder and the underlying material.

Contributing factors may include high scanning speeds, low laser power, inadequate track overlap, or uneven powder distribution, all of which result in shallow melt pools. Lack-of-fusion defects are characterised by irregular and angular voids that indicate areas where melting did not occur.
In some instances, lack of fusion may coexist with cold cracking, while in others, keyhole porosities may be more prevalent. This emphasises the necessity for optimisation of process parameters to mitigate the occurrence of these defects.

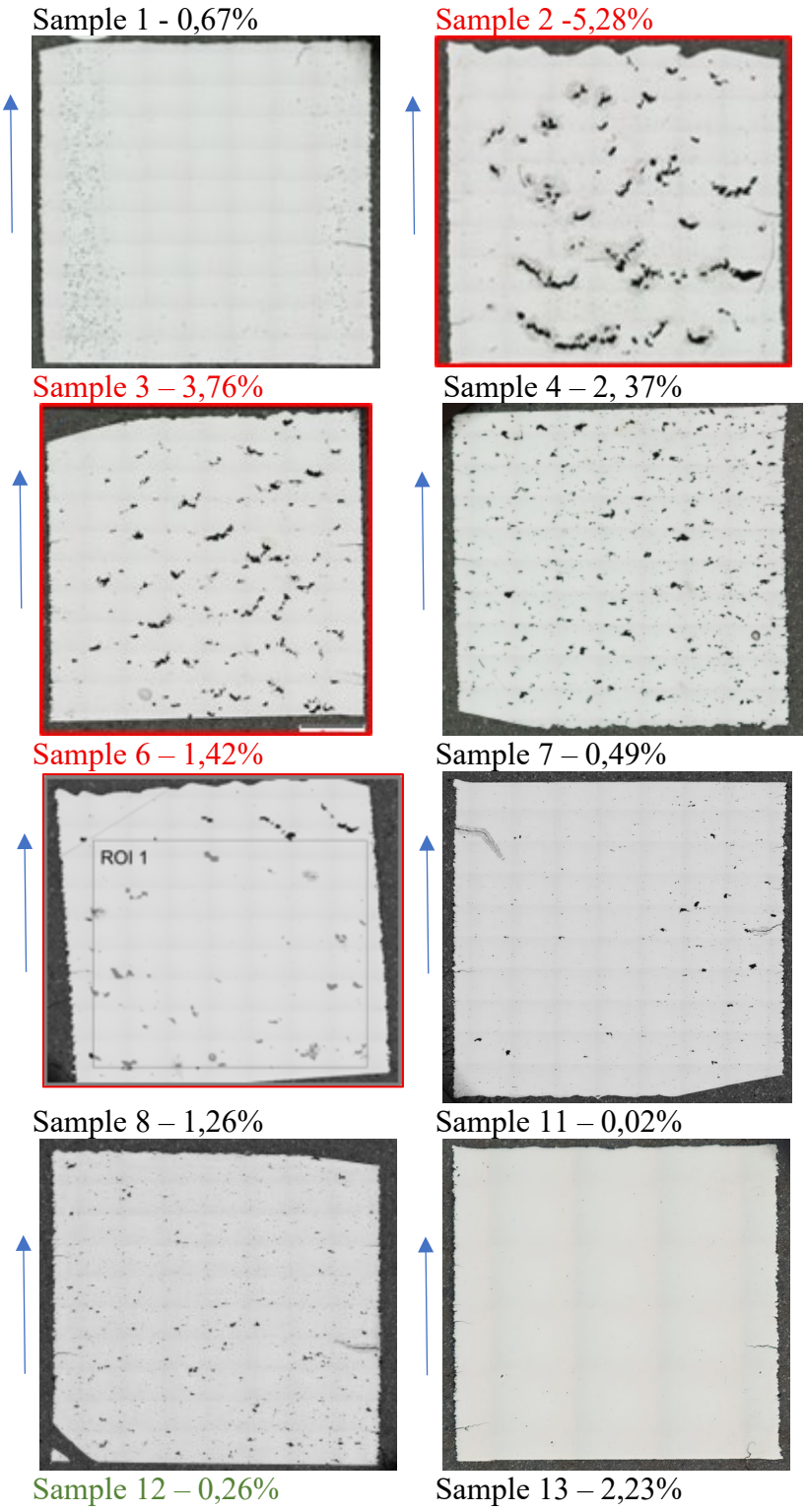

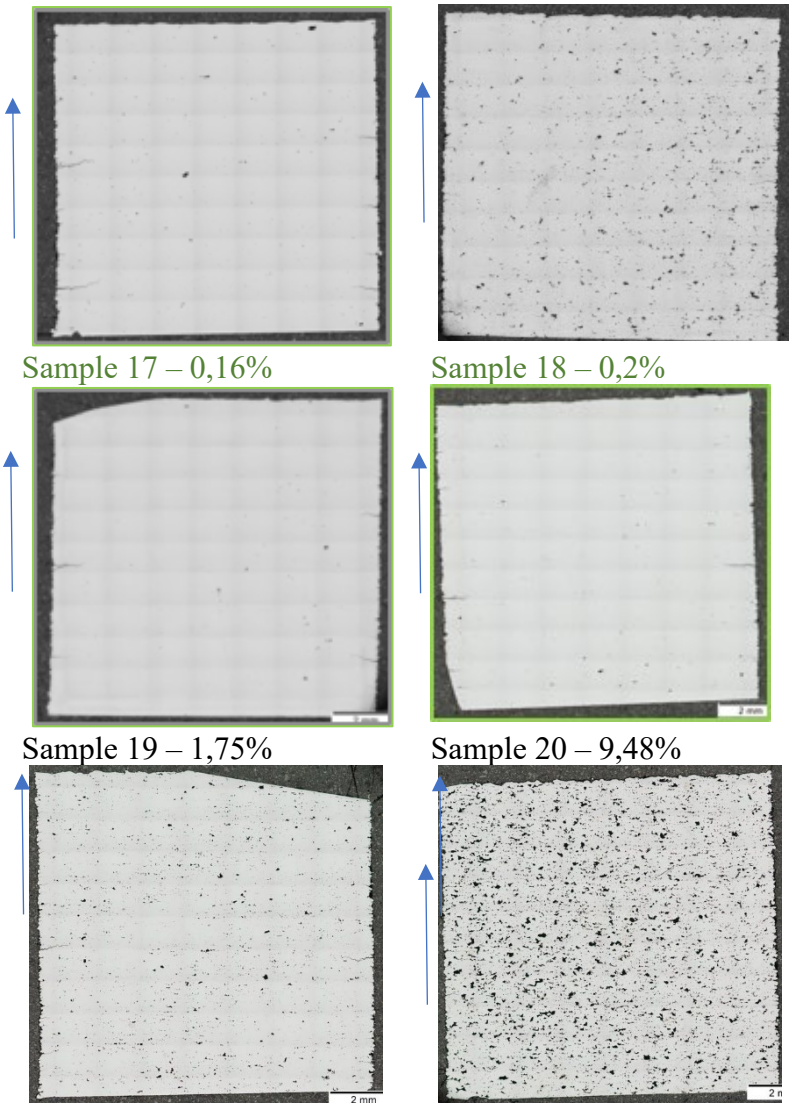

Fig. 3. Optical micrographs of the cross sections showing the porosity and highlighting the worst (red) and best (green) roughness measurements (Figure 1). The arrows show the building direction.

Influence of alloying elements on the processing map

Figure 4 illustrates the processing maps for both tool steels S2 and S6, showing the regions associated with different defect as well as the zone for process stability. The printing parameters in S6 were observed to be lower than those in S2, which can be attributed to the differing characteristic of the two printers employed. Additionally, for S6 tool steel, the processing map exhibits a "not finished" window for some samples, in relations to interruptions of the printing process caused by excessive spatters. In both S2 and S6 grades, lack-of-fusion occurs at low laser powers and high scan speeds, while excessive energy input - particularly at high power and low scan speeds - leads to keyhole formation and spatter. However, the location and extent of these defect windows differ markedly between the two alloys.

Focusing on the optimal processing window, the area that enables the production of fully dense and defect-free samples is noticeably larger for S2 than for S6. In S2, a broad range of power–scan speed combinations results in stable melting behaviour with limited porosity or cracking. By contrast, the processing window for S6 is significantly more restricted, shifting toward higher power and scan speeds, particularly between 200 W and 100–1200 mm/s. At reduced power levels (e.g., 125 W), the lack-of-fusion region widens considerably in S6, especially at higher scan speeds, indicating a much lower tolerance for variations in energy input.

The differences in window size and processability are closely linked to alloying content. S6 contains substantially higher levels of Cr, V, Si, and Mn, which promote micro segregation, broaden the

solidification range, and encourage the formation of interdendritic carbide networks [18]. These features increase susceptibility to cracking, porosity, and melt-pool instability, ultimately limiting the feasible parameter space [5, 19]. In contrast, the lower alloying content in S2 reduces segregation and minimises the development of brittle eutectic or carbide-rich regions, resulting in a more stable melt pool and greater robustness against parameter fluctuations.

Overall, Figure 3 demonstrates that increasing alloying complexity in LPBF tool steels directly affects process stability and defect formation. Alloys such as S6 therefore require tighter parameter control and potentially additional measures—such as in-situ heating—to mitigate cracking and expand the usable processing window, as suggested for highly alloyed steels by recent studies [19, 20].

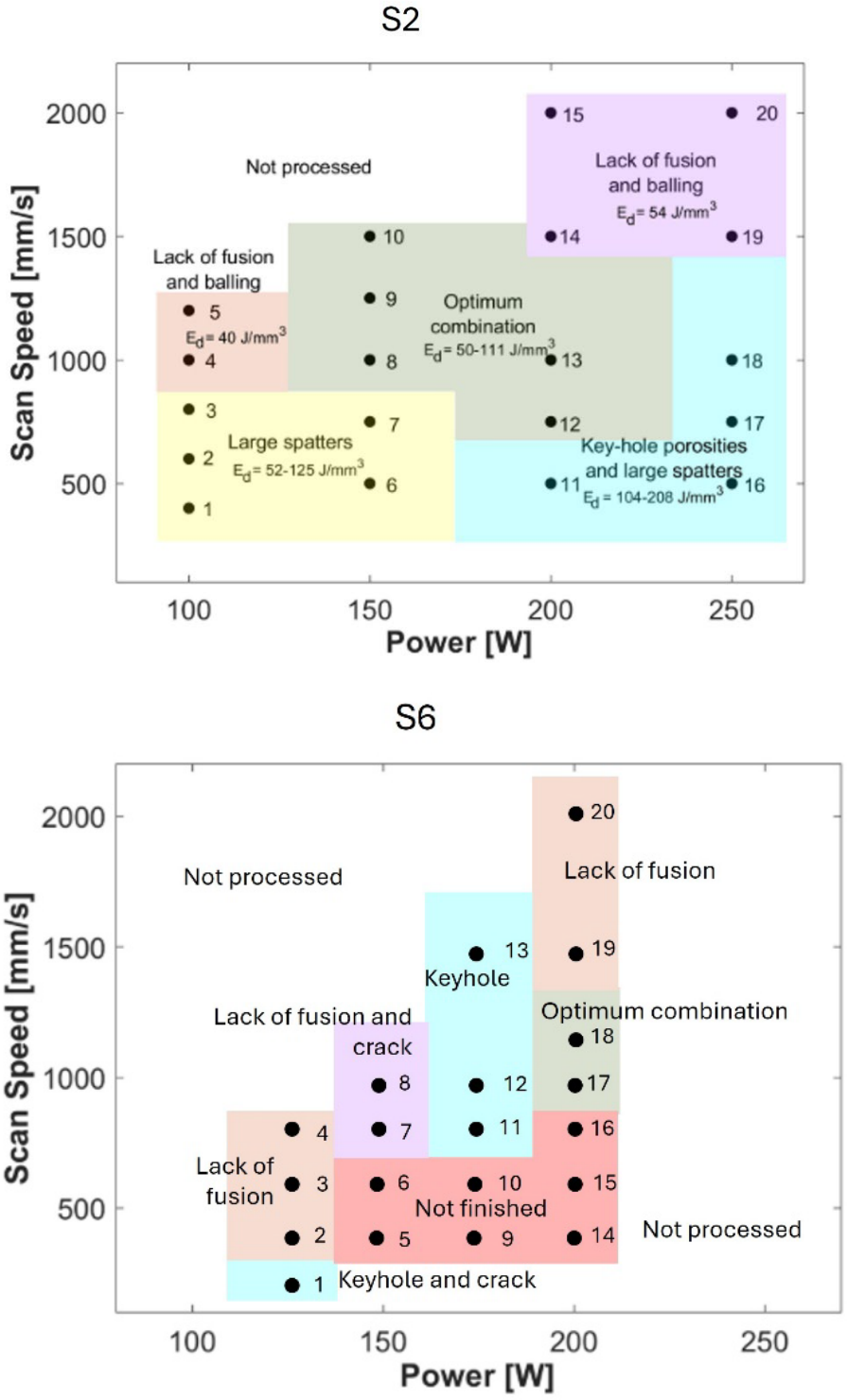

Fig. 4. Process map of LPBF S2 tool steel (up) and S6 tool steel (below).

Conclusion

The present study investigates the laser powder bed fusion (LPBF) process applied to S6 tool steel cubes, with the objective of identifying the optimal processing parameters through systematic variation of key factors, particularly laser power and scanning speed.
Characterisation and classification of surface roughness and internal defects within the fabricated samples were conducted to evaluate the impact of these variables.
Furthermore, to elucidate the influence of alloying elements, the LPBF process window established for S6 tool steel was juxtaposed with that derived from a similar but distinct S2 tool steel.
The defects observed in the non-optimal processing zones were found to be analogous for both steel types. However, it is posited that the elevated concentrations of alloying elements in the S6 steel may either enhance micro-segregation and the formation of carbide networks or broaden the solidification range.
Ultimately, the findings indicate that the optimal processing window for S6 tool steel is more constrained in comparison to S2, with a shift towards higher laser powers and scanning speeds attributable to the differing alloy compositions. Future work will investigate the possible segregation and local variation of the microstructure.

Acknowledgement

This work was supported by the FNRS (Fonds National de la Recherche Scientifique of Belgium, PDR number 35298295). The authors also acknowledge the help of Sylvie Salieri for sample preparation.

References

[1] S. Ramadurga Narasimharaju, W. Zeng, T. Long See, Z. Zhu, P. Scott, X. Jiang (Jane) & S. Lou: submitted to Journal of Manufacturing Processes (2022).

[2] H. Zong, N. Kang, M. El Mansori: submitted to Journal of Nano Materials Science (2025).

[3] S. A. Khairallah, A. T. Anderson, A. Rubenchik, W. E. King: submitted to Journal of Acta Materalia (2016).

[4] N. Hantke, F. Großwendt, A. Strauch, R. Fechte-Heinen, A. Röttger, W. Theisen, S. Weber, J. T. Sehrt: submitted to Journal fo Materials (2022).

[5] Y. Wu, L. Yang: submitted to International Journal of Mechanical Science (2021).

[6] G. Huang, K. Wei, J. Deng, M. Liu, X. Zeng: submitted to Journal of Manufacturing Processes (2022).

[7] F. Galbusera, A. G. Demir, J, Platl, C. Turk, R, Schnitzer, B, Previtali: submitted to Journal of Material Processing Techonology (2022).

[8] Yadroitsev, I., & Smurov, I: submitted to Journal of Physics Procedia (2010).

[9] F. Bahari-Sambran, A. Orozco-Caballero, F. Carreño, C.M. Cepeda-Jiménez: submitted to Journal of Advances in Industrial and Manufacturing Engineering (2025).

[10] S. A. Khairallah, A. T. Anderson, A. Rubenchik,W. E. King: submitted to Journal of Acta Materialia (2016).

[11] W. E. King, H. D. Barth, V. M. Castillo, G. F. Gallegos, J. W. Gibbs, D. E. Hahn, C. Kamath, A, M. Rubenchik: submitted to Journal of Materials Processing Technology (2015).

[12] Frazier W. E: submitted to Journal of Materials Engineering and Performance (2014).

[13] E. Saggionetto, E. Filippi, O. Dedry, J. Tchuindjang, A. Mertens: submitted to Materials Research Proceedings (2023).

[14] W. E. King, H. D. Barth, V. M. Castillo, G. F. Gallegos, J. W. Gibbs, D. E. Hahn, C. Kamath, A. M. Rubenchik: submitted to Journal of Materials Processing Technology (2014).

[15] J. Platl, H. Leitner, C. Turk, A. G. Demir, B. Previtali, R. Schnitzer: submitted to Journal of Advanced Engineering Material (2020).

[16] T. Sun, Z. Wang, Q. Wie, Y. Wu, M. Wang, L. Kong: submitted to Journal of Metallurgical and Materials Transsaction A (2024).

[17] D. Guillen, S. Wahlquist, A. Ali: submitted to Journal of Applied Science (2024).

[18] M. Vilanova, M. C. Taboada, A. Martinez-Amesti, A. Niklas, M. S. Sebastian, T. Guraya: submitted to Journal of Materials (2021).

[19] J. Kunz, M. L. Köhler, S. Herzog, A. Kaletsch, C. Broeckmann: submitted to Journal of Steel Research International (2021).

[20] S. Bergmuellera, L. Kaserera, L. Fuchsa, J. Brauna, N. Weinbergerb, I. Letofsky-Papstc, G. Leichtfried: submitted to Journal of Helyion (2022).